# Title: Core neurons are structural crossroads of cortical dynamics

**Authors:** Domenico Guarino[1]*, Anton Filipchuk[1,2], Alain Destexhe[1]*.

**Affiliations:**

[1] Department for Integrative and Computational Neuroscience (ICN), Paris-Saclay Institute of Neuroscience (NeuroPSI); Campus CEA Saclay, 151 route de la Rotonde, Bâtiment 151, 91400 Saclay, France.

[2] ICM, Institut du cerveau, Hôpital Pitié, 47 Bd de l'Hôpital, 75013 Paris.

*Corresponding author. Email: domenico.guarino@universite-paris-saclay.fr, alain.destexhe@cnrs.fr

**Abstract**: Cortical events of correlated neuronal firing are thought to underlie sensorimotor and associative functions. In the dominant theory, events are attractors of cortical dynamics, pulled by strong mutual connections between recurrently active – core – neurons. Here, we exhaustively measured core connectivity, using a unique dataset with co-registered two-photon calcium imaging and electron microscopy of the same cortical tissue. We report that cores make fewer, weaker, mutual connections compared to other neurons. Instead, cores are central to the flow of the many pathways they belong to. We present a model where cores arise from a simple distance-dependent connectivity rule, without imposed connectivity biases. Our integrated analysis shows that the link between cortical dynamics and structure is not consistent with attractors but rather with confluent connectivity pathways.

**One-Sentence Summary:** Recurrently active within reproducible population events, core neurons characterize cortical activity not by virtue of strong mutual connections but by being central to many crossing pathways.

**Main Text:**

According to Hebb (*1,2*), thought processes and behaviors correspond to the activation of *cell assemblies* – sets of neurons connected such that once a subset fires, the rest will fire. Their specificity and reliability would come from strengthening connections between experience-driven coactive neurons. Hopfield (*3*) proposed a computational model describing this, where strengthening connections between input-driven coactive units creates *attractors* – reproducible activity patterns reliably associated with stimulus patterns. This model has become a cornerstone of cortical dynamics (*4*), although convincing experimental evidence is available only for the hippocampus (*5*). Attractor-based models of cortical dynamics can be experimentally tested today, thanks to optical physiology. Two-photon calcium imaging of the awake mouse cortex shows synchronous irregular population events, also called ensembles (*6*) or neural assemblies (*7*). These events are selectively evoked by stimuli, recur under the same stimulus presentations, keep their specificity also when recurring spontaneously (*7–9*), and can be induced by repetitive coactivation (*10*). All these characteristics have reinforced the idea that population events are the result of local attractor networks (*6, 8–11*).

One particular feature of population events can help settle the matter. Recurring population events do not repeat identically. Their unifying feature is *core* neurons, subsets reliably participating in all event occurrences (*7, 8, 11*). Following the attractor paradigm, cores have been considered as biological equivalents of *pattern completion* units – capable of pulling the network dynamic towards a stored attractor, by virtue of strong mutual connections (*11, 18*). However, recent experiments show that repeated optogenetic co-activations do not strengthen synapses, rather they increase cell excitability (*12*). Also, strong connections are theoretically associated with non-transient attractor states (*13*), slowing of network dynamics (*14*), and pathological run-away activity (*15*), which require counter-balancing solutions (*16, 17*).

Here, we present evidence contrasting the hypothesis that core neurons are strongly connected. In particular, we variously tested two fundamental attractor-driven assumptions: (i) *synapses between cores are more efficient compared to others*, and (ii) *circuits made by cores involve more recursive connections toward cores* (*3, 11, 18*). We found that cores do not make either more efficient or more recursive mutual connections. Instead, the essential characteristic of core neurons is being the confluence of many pathways.

To perform the tests, we needed information about both the *firing* of neurons, to identify events and cores, and the *connections* of those same neurons, to perform structural analysis of the circuits in which the cores were embedded. Until recently (*19*), this double requirement was impossible to fulfill. The MICrONS project (*20*) gives a unique opportunity, publicly releasing electron microscopy (EM) and co-registered two-photon calcium imaging datasets of the same cortical tissue (Fig. 1A). Only one dataset had the temporal resolution to perform core analysis. But its duration (1850 sec, at ~14.8 Hz) and structure (187 cells with both EM reconstruction and two-photon recording, with 1962 proofread synapses) warranted statistical analyses. Furthermore, we verified the two-photon dataset generality against ($N$=32) recordings from the Allen Brain Observatory (*21*).

To identify recurrent spiking patterns, and their core neurons, we expanded a previously described method (*7, 32*) for the analysis of two-photon calcium imaging rasters (Fig. 1B). Briefly, a population event was identified as a peak of synchronous firing, beyond a surrogate-based significance threshold (Fig. 1C). The neurons firing within an event were listed in a vector (Fig. 1B, left). The re-occurrence of neurons across events was then used to gather

reproducible patterns into correlation-based clusters (Fig. 1D). Finally, core neurons were singled out as those participating in (>95%) events of each cluster (Fig. 1D, inset).

The MICrONS two-photon dataset presented 227 significant events, 43 events made 7 clusters of significant reproducibility, with 33 core neurons and 154 non-core neurons, evenly occurring along events (Fig. 1E and F). The number of events, their pattern reproducibility, and the timing of core occurrences were similarly distributed in the MICrONS and Allen Brain Observatory datasets (Fig. S1).

Once cores were singled out, we proceeded with testing the attractor-driven assumptions. For the first – *synapses between cores are more efficient compared to others* – we took the number and volume of postsynaptic spines as proxies for synaptic efficacy (*21-24*). For each event, we took the distribution of spines between the identified cores and all other neurons (Fig. 2A). We found few core-to-core spines, but many core-to-other, other-to-core, and other-to-other spines. Besides, the postsynaptic spine volume of core neurons was significantly smaller than all others, with medium to high effect size (see Fig. 2A for Kruskal-Wallis tests and Kolmogorov-Smirnov magnitudes, *KS*). Other neurons, either within or beyond the EM volume, made a large number of spines on cores and other neurons too (Fig. 2A, left), but they were on average not bigger than local spines, and they were not part of the two-photon dataset, therefore we did not integrate them in further analyses.

Core to core connection efficacy might also have been due to (unspecified) factors other than spine volume. To address this possibility, we used a commonly performed connectivity estimate based on 1-lag spiking correlations between neurons (*25*, and Fig. S2). Again, the resulting correlations were significantly lower between cores compared to all others, with a small *KS* effect size (Fig. 2B).

For the second assumption to test – *circuits made by cores involve more recursive connections towards cores* – we performed several graph theory analyses. To get a global picture of mutual connectivity, we looked at the distribution of motifs – statistically significant connectivity patterns considering groups of three cells (*26*). To understand the significance of motif occurrences, we used the ratio of real and 100 surrogate degree-matched network distributions (*27*). The ratio showed an abundance of mutual motifs (Fig. 2C). However, looking at the motif distribution as a function of cores and other neurons, across all population events, we found that mutual connections were not specific to cores but were abundant for both cores and other neurons, as well as convergent and divergent motifs (Fig. 2D). This was also confirmed by the assortativity coefficient $r$ for the whole network – the connection correlation between cell types (either 'core' or 'other'). Assortativity would be $r$=1 if all connections joined the same type, and $r$=-1 if all their connections joined the opposite type. We found $r$=0.092, characteristic of non-preferentially connected networks.

Even if not having prevailing direct and mutual connections, the core mutual activity could be sustained by indirect synaptic feedback, via secondary or looped pathways, abundant enough to ensure that they were pattern completion units in traditional attractor network terms (*18*). To check both possibilities, we measured the number and length of shortest paths and cycles between cores or non-cores. Neither gave a significant advantage to cores (Fig. S3).

The relative abundance of convergent and divergent motifs suggested that core neurons could be central to many cortical pathways. To assess how much, we took six well-established graph centrality measures: degree, betweenness, eccentricity, closeness, flow and authority/hub scores, which look at centrality from different angles.

The degree – number of connections – is a direct measure of a neuron's importance in the network. Cores had significantly more connections than others (Fig. 2E).

A more specific measure of a neuron centrality is its betweenness – the number of paths between two other nodes a neuron lies upon. Core betweenness was significantly higher than non-core neurons (Fig. 2F).

Not only cores were lying onto many pathways, but longer ones too. Their eccentricity – the maximal average shortest path to any other neuron - was significantly longer than non-cores (Fig. 2G), and also longer than the average network path length (3.68 neurons).

Being on many long pathways, cores easily reached more neurons than non-cores. Their closeness centrality – here measured as the (harmonic) mean inverse distance between cells – was significantly higher than other neurons (Fig. 2H).

Finally, to understand how core centrality could affect population events, we considered the flow – number and identity of connections to cut to interrupt the circuit between the first and the last firing neuron of each population event (e.g. the subgraphs made by neurons active in the events depicted in Fig. 1E). Core neuron connections were responsible for blocking more than twice event flows as non-cores (Fig. 2I). This was confirmed by looking at the authority and hub centrality – which assign scores to a neuron proportional to the scores of the neurons it is connected by. Core neurons had significantly higher authority and hub scores than others (Fig. 2J).

Altogether, there were neither more strong nor recursive connections between cores. But they were central to the confluence of pathways into population events. Then, if not strong connections, what is the connectivity principle leading to reproducible activity patterns and core neurons?

Based on the strong connectivity assumption, models have been proposed where strong recursive paths were arbitrarily imposed on randomly connected networks (*28*) by either additional circuits or increased synaptic strength within arbitrarily selected neurons (*11, 28, 29*). However, the predictive power of these models, concerning recurrent population events, is diminished by their ad-hoc solutions (*2*).

Here, we present a conductance-based balanced network model where the presence of core neurons results only from a distance-dependent connection strategy. In building our model, we established connections for each cell by randomly sampling its neighborhood with probability exponentially decreasing for increasing distances. We chose parameters such that connectivity loosely followed the EM distribution of distances and degrees (Fig. S4). And we assigned the same synaptic efficacy to all connections, to eschew the first attractor-driven assumption (and we tested results stability under several synaptic conductance values, Fig. S5). For model cell dynamics, we used already published parameters from mouse cortex (*30*). The model was driven by external independent Poisson spike generators (proportional in number to Fig. 2A non-local synapses).

The model produced synchronous irregular population events (Fig. 3A, B), onto which we applied the same core analysis as above (Fig. 3C), giving 407 significant events, of which 273 made 8 clusters of significant reproducibility, with 176 core cells evenly occurring across events (Fig. 3D, E).

We then proceeded to test the second attractor-driven assumption: core connections recursiveness. The distance-dependent connection strategy was sufficient to get core vs other

distributions for degree, betweenness, and flow, resembling in significativity and effect size the relationships found in the MICrONS dataset (Fig. 3F-I). As in that dataset, the model presented no evidence of more mutual connectivity via indirect synaptic feedback for cores (Fig. S6). The distance-dependent connection strategy was also necessary. When the same network was randomly rewired, preserving node degrees, it gave rise to population events, but no reproducible pattern was identified, and consequently no cores (Fig. S7).

Our modeling confirmed that locally clustered (here via distance-dependent) connectivity produces weakly recursive circuits that irregularly transition between periods of higher and lower firing rates (*29, 31, 32*). Importantly, we add that distance-dependent connection clustering is also the source of population event reproducibility and cores.

One major limitation of our study is that a single mouse dataset necessarily gives a biased picture. Yet, the coordinated EM/two-photon approach will generate more datasets, improving the present picture, provided that a high temporal resolution is kept in future datasets. In addition, we supply a conservative model mimicking structural and dynamical experimental features. This model closed in all structural measures of the real cortex it was compared to. Besides, the general distance-dependent strategy we adopted is also susceptible to varying sampling distributions beyond exponential (*32*).

Hebb's assemblies were made of sparse circuits spanning the whole cortex (1, 2). Hopfield's attractor implementation was efficient and narrowed their definition in space. It was also specific enough to become experimentally testable (*10*). Cortical uniformity and modularity have been used to argue for a local attractor-like nature of cortex (*2, 4, 11*). This implies that local portions of cortex showing dynamic signs of being attractors, like reproducible population events, should also hold structural traces of being attractors. Our data analysis and modeling integration showed that cortical core neurons are not attractor network units. Instead, they sit at the confluence of many pathways. Our work contributes to restoring Hebb's initial idea: assemblies might fit an attractor definition, but not a local one.

**References and Notes**


1. D. O. Hebb, *The organization of behavior: A neuropsychological theory* (Psychology Press, 2005).
2. R. Yuste, From the neuron doctrine to neural networks. *Nature reviews neuroscience, **16*** (8), 487-497 (2015).
3. J. J. Hopfield, Neural networks and physical systems with emergent collective computational abilities. *Proc. Natl. Acad. Sci. U.S.A., **79***, 2554-2558 (1982).
4. D. L. Barack, J. W. Krakauer, Two views on the cognitive brain. *Nature Reviews Neuroscience, **22***, 359-371 (2021).
5. T. Wills et al., Attractor Dynamics in the Hippocampal Representation of the Local Environment. *Science, **308*** (5723), 873–876 (2005).
6. R. Cossart, Y. Ikegaya, R. Yuste, Calcium imaging of cortical networks dynamics. *Cell calcium, **37***, 451-457 (2005).

7. A. Filipchuk, A. Destexhe, B. Bathellier, Awake perception is associated with dedicated neuronal assemblies in cerebral cortex. https://www.biorxiv.org/content/10.1101/2021.08.31.458322v1 (2021).

8. J. Miller, I. Ayzenshtat, L. Carrillo-Reid, R. Yuste, Visual stimuli recruit intrinsically generated cortical ensembles. *Proc. Natl. Acad. Sci. U.S.A.*, **111**, E4053-E4061 (2014).

9. L. Carrillo-Reid, S. Han, W. Yang, A. Akrouh, R. Yuste, Controlling visually guided behavior by holographic recalling of cortical ensembles. *Cell, **178***, 447-457 (2019).

10. L. Carrillo-Reid, W. Yang, Y. Bando, D. Peterka, R. Yuste, Imprinting and recalling cortical ensembles. *Science, **353***, 691-694 (2016).

11. L. Carrillo-Reid, S. Han, D. O'Neil, E. Taralova, T. Jebara, R. Yuste, Identification of Pattern Completion Neurons in Neuronal Ensembles Using Probabilistic Graphical Models. *Journal of Neuroscience, **41***, 8577-8588 (2021).

12. A. Tzitzitlini, S. Kim, J. Pérez-Ortega, R. Yuste, Intrinsic excitability mechanisms of neuronal ensemble formation. https://www.biorxiv.org/content/10.1101/2020.07.29.223966v2 (2020).

13. Y. Wu, F. Zenke, Nonlinear transient amplification in recurrent neural networks with short-term plasticity. *Elife, **10***, e71263 (2021).

14. S. Sadeh, C. Clopath, Inhibitory stabilization and cortical computation. *Nature Reviews Neuroscience, **22***, 21-37 (2021).

15. D. Zhang, *et al.*, Global enhancement of cortical excitability following coactivation of large neuronal populations. *Proc. Natl. Acad. Sci. U.S.A. **117***, 20254-20264 (2020).

16. C. van Vreeswijk, H. Sompolinsky, Chaos in neuronal networks with balanced excitatory and inhibitory activity. *Science, **274***, 1724-1726 (1996).

17. S. Denève, C. Machens, Efficient codes and balanced networks. *Nature neuroscience, **19***, 375-382 (2016).

18. E. T. Rolls, Attractor networks. WIREs Cognitive Science, 1, 119–134 (2010).

19. D. Bock, et al. Network anatomy and in vivo physiology of visual cortical neurons. *Nature, **471***, 177-182 (2011).

20. S. Dorkenwald et al. Binary and analog variation of synapses between cortical pyramidal neurons. https://doi.org/10.1101/2019.12.29.89031 (2019).

21. S. de Vries, et al. A large-scale standardized physiological survey reveals functional organization of the mouse visual cortex. *Nature Neuroscience **23***, 138–151 (2020).

22. A. Vanharreveld, E. Fifkova, Mechanism for potentiation and short-term memory. *Proceedings of the Koninklijke Nederlandse Akademie, **78***, 21-24 (1975).

23. M. Matsuzaki, et al. Dendritic spine geometry is critical for AMPA receptor expression in hippocampal CA1 pyramidal neurons. *Nature neuroscience, **4***, 1086-1092 (2001).

24. S. Barnes, et al.. Deprivation-induced homeostatic spine scaling in vivo is localized to dendritic branches that have undergone recent spine loss. *Neuron, **96***, 871-882 (2017).

25. A. Sadovsky, J. MacLean, Scaling of topologically similar functional modules defines mouse primary auditory and somatosensory microcircuitry. *Journal of Neuroscience, **33***, 14048-14060 (2013).

26. R. Milo, *et al.*, Network motifs: simple building blocks of complex networks. *Science, **298***, 824-827 (2002).

27. S. Song, *et al.*, Highly nonrandom features of synaptic connectivity in local cortical circuits. *PLoS Biology, **3***, e68 (2005).

28. T. Vogels, L. Abbott, Signal propagation and logic gating in networks of integrate-and-fire neurons. *Journal of Neuroscience, **25***, 10786-10795 (2005).

29. A. Litwin-Kumar, B. Doiron, Slow dynamics and high variability in balanced cortical networks with clustered connections. *Nature Neuroscience, **15***, 1498-1505 (2012).

30. Y. Zerlaut, *et al.*, Heterogeneous firing rate response of mouse layer V pyramidal neurons in the fluctuation driven regime. *The Journal of physiology, **594***, 3791-3808 (2016).

31. P. Yger, *et al.*, Topologically invariant macroscopic statistics in balanced networks of conductance-based integrate-and-fire neurons. Journal of computational neuroscience, 31, 229-245 (2011).

32. S. Spreizer, A. Aertsen, A. Kumar, From space to time: Spatial inhomogeneities lead to the emergence of spatiotemporal sequences in spiking neuronal networks. *PLoS computational biology, **15***(10), e1007432 (2019).

33. Materials and methods are available as supplementary materials at the Science website.

**Methods references**

34. G. Csárdi, T. Nepusz, The igraph software package for complex network research. Inter *Journal Complex Systems, **1695*** (2006).

35. D. Kätzel, B. Zemelman, C. Buetfering, M. Wölfel, G. Miesenböck, The columnar and laminar organization of inhibitory connections to neocortical excitatory cells. *Nature Neuroscience, **14***, 100-107 (2011).

36. H. Markram, et al. Reconstruction and simulation of neocortical microcircuitry. *Cell, **163***, 456-492 (2015).

37. S. C. Seeman, et al. Sparse recurrent excitatory connectivity in the microcircuit of the adult mouse and human cortex. *Elife, **7***, e37349 (2018).

38. M. Diesmann, M. Gewaltig, NEST: An environment for neural systems simulations. *Forschung und wisschenschaftliches Rechnen, Beiträge zum Heinz-Billing-Preis, **58***, 43-70 (2001).

39. A. Davison et al., PyNN: a common interface for neuronal network simulators. *Frontiers in neuroinformatics, **2***, 11, (2009).

**Acknowledgments:** We express our gratitude to the MICrONS project and the Allen Brain Institute for the efforts they make and their commitment to publicly releasing painstakingly

collected datasets, without which this study would have not been possible. We would like to thank Federico Tesler and Manuel Mameli for stimulating discussions and critically reading the manuscript. The mouse drawing in Fig. 1 is gently offered by Ethan Tyler and Lex Kravitz.

**Funding:**

EC Human Brain Project (HBP, grant agreement no. H2020-945539).

**Author contributions:**

Conceptualization: DG, AF, AD

Methodology: DG, AF

Investigation: DG, AF, AD

Visualization: DG, AF

Funding acquisition: AD

Project administration: AD

Supervision: AD

Writing – original draft: DG, AF, AD

Writing – review & editing: DG, AF, AD

**Competing interests:** Authors declare that they have no competing interests.

**Data and materials availability:** All data, code, and materials used in the analysis are publicly available to any researcher for purposes of reproducing or extending the analysis. The MICrONS project dataset is available at: https://www.microns-explorer.org/phase1. The Allen Brain Observatory dataset is available at: http://observatory.brain-map.org. The calls to retrieve the data are listed in the Materials and Methods section. The code to run all analyses and simulations is available at https://github.com/dguarino/2photon and https://github.com/dguarino/tessera. Two docker images (to avoid the setup of data analysis and simulation environments) are also available at https://hub.docker.com/r/dguarino/2photon and https://hub.docker.com/r/dguarino/neuro.

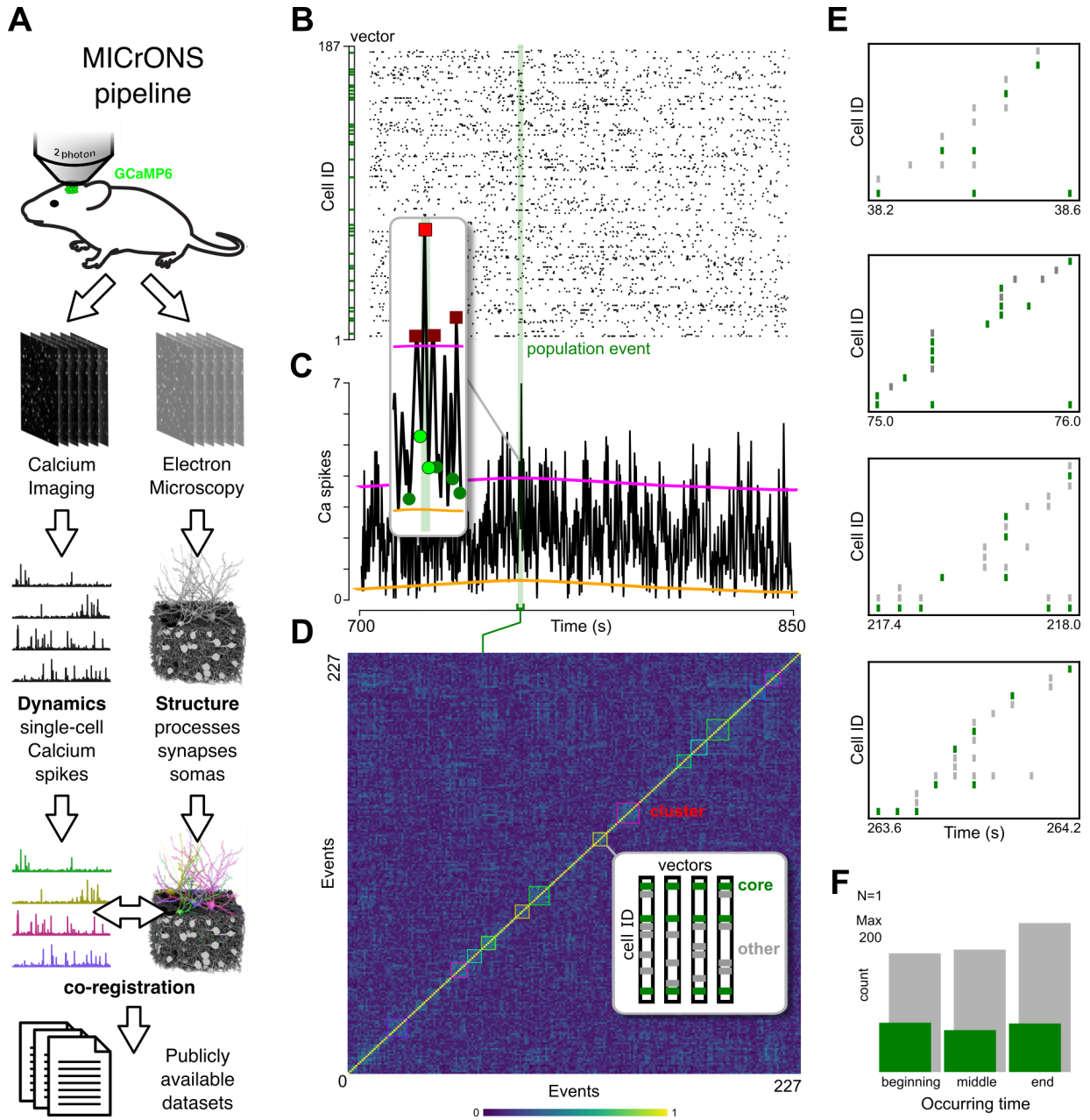


**Fig. 1. Core neurons fire all along population events.** (**A**) Schematic diagram of the MICrONS pipeline. In-vivo calcium imaging and serial EM imaging were performed on the same mouse cortical volume, yielding electrophysiological dynamics and spatial structure of neurons and synapses. An automatized co-registering procedure matched each neuron visible in the calcium imaging movie with a corresponding neuron in the anatomical EM stack. After human curation, the data was released to the public. (**B**) Calcium spikes raster plot from awake mice of the MICrONS dataset. Fluctuations in spike frequency are synchronous population events (green shade). (**C**) Population events were quantified as time intervals where the firing rate (black) exceeded a surrogate-based threshold (magenta) above firing baseline (orange). *Inset*. The subthreshold beginning and end of each event were the minima (green points) before and after each peak (red squares). Each event was assigned a population binary vector (panel A, participating cells in green). (**D**) Each population binary vector was correlated with all others

(color intensity reflects the degree of correlation) and clustered based on their correlation proximity. Population events sharing neurons beyond a surrogate-based threshold were identified (colored squares), their autocorrelation computed, and the cells participating in 95% of their events were labeled as “cores” (Right, inset). (**E**) Example events from the dataset. Cells are displayed sorted by time of occurrence. (**F**) Core neurons (green) were evenly distributed along events.

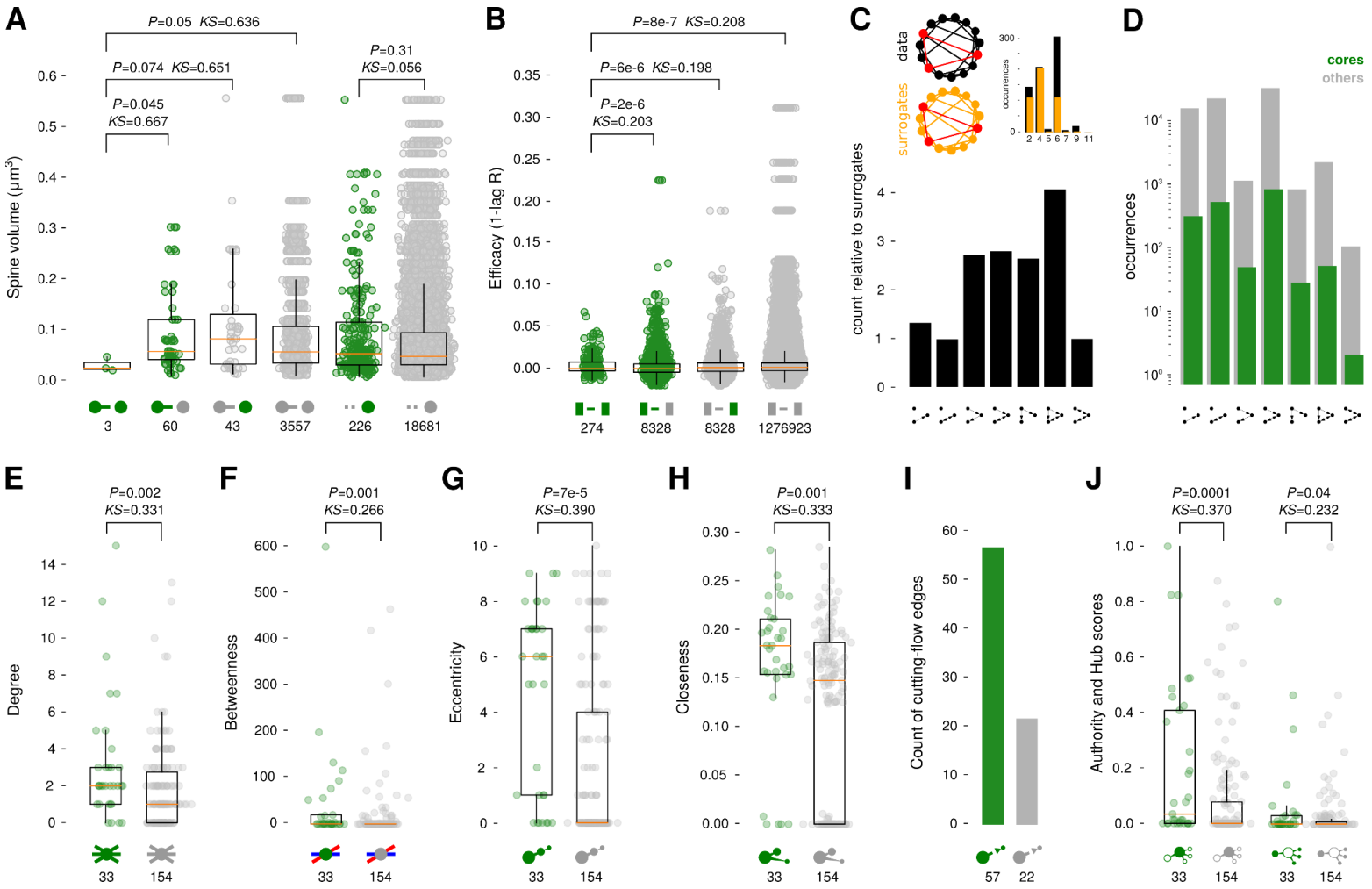


**Fig. 2. Core neurons are crossroads of cortical structure and dynamics.** (**A**) Postsynaptic spine volume was significantly lower for synapses between core neurons (circles: measured spines), compared to the spines made by any combination of cores (green) and others (gray). (*Left*) Spines from neurons beyond the scanned tissue were more (twice for cores, six times for others). (**B**) Connection efficiency (1-lag firing correlation) was significantly lower between cores, compared to any other combination of cores and others. (**C**) EM connectivity motifs distribution for all two-photon recorded neurons (**top**: all motifs, numbered for clarity, exceeded surrogate networks). (**D**) Motif occurrence distribution for cores (green) and other (gray) neurons (count for each reproducible cluster). Both cores and other neurons made a mixture of mutual and non-mutual connections. (**E**) Core neurons had a larger number of connections compared to other non-cores. (**F**) Core neurons were on significantly more pathways than others. (**G**) Cores reached significantly further than others. (**H**) Cores had significantly smaller (higher inverse) distance to all neurons compared to non-cores. (**I**) Removing core connections stopped more flows from beginning to end of an event subnetwork. (**J**) Core neurons had significantly higher authority (left) and hub (right) scores than non-cores.

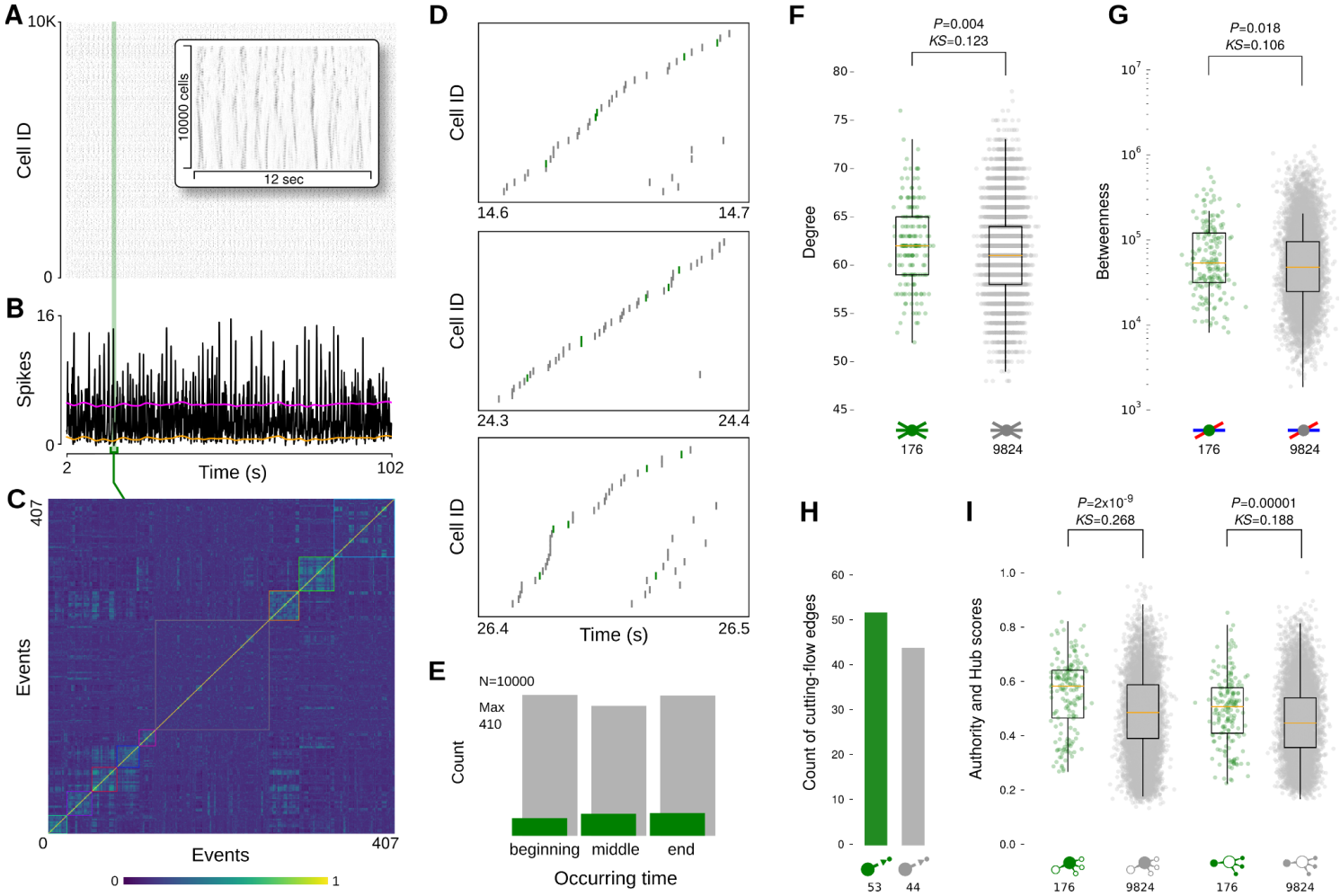


**Fig. 3. A spiking model reproduces in-vivo core features.** (**A**) Spikes raster plot with synchronous population events (green shade) with detail in time (**inset**, time expansion to appreciate event dynamics). The model was made of 10000 excitatory and 2500 inhibitory adaptive-exponential integrate-and-fire point neurons on a grid covering approximately 500µm with units separated by 5 µm. The model showed a dynamic similar to that observed in cortical activities (see Methods). (**B**) Population events were quantified as in fig. 1A. (**C**) Population binary vectors were correlated with all others and clustered as in fig. 1C (gray squares identify non-significant clusters). (**D**) Example events from the model. (**E**) Core neurons (green) were evenly distributed along events. (**F**) Core neurons had a larger number of connections compared to other non-cores. (**G**) Core neurons were on significantly more pathways than others. (**H**) Removing core connections stopped more flows from beginning to end of event subnetworks. (**I**) Core neurons had significantly higher authority (left) and hub (right) scores than non-cores.

Supplementary Materials for

# Core neurons are structural crossroads of cortical dynamics

Domenico Guarino, Anton Filipchuk, Alain Destexhe

Correspondence to: domenico.guarino@universite-paris-saclay.fr, alain.destexhe@cnrs.fr

**This PDF includes:**

Materials and Methods

Fig. S1 to S7

## Materials and Methods

We performed the same structural and dynamical analyses over data collected in mouse cortex and in biologically constrained conductance-based spiking models. All animal procedures were in accordance with the Institutional Animal Care and Use Committees at the Baylor College of Medicine and the Allen Institute for Brain Science.

**MICrONS data source**. The MICrONS project (https://www.microns-explorer.org/) made available, through its website, two datasets, corresponding to the first two phases of the project. The first phase, the one we used, has electron microscopy and functional imaging of the same cortical patch of V1, in a 400✕400✕200 μm volume with the superficial surface of the volume at the border of L1 and L2/3, approximately 100μm below the pia. Here follows a brief description of the procedures, and we refer the interested reader to Dorkenwald et al. 2019. **Two-Photon imaging**. Functional imaging was performed in a transgenic mouse expressing fluorescent GCaMP6f from the Jackson Laboratories (jax.org) and the Allen Brain Institute (see next section on the Allen data source). The complete description of mouse transgenic line, surgical procedures, implants, two-photon microscope features, stimulation and recording setups, and protocols were already published (Dorkenwald et al. 2019). One important feature and the main difference with the Allen Brain Observatory two-photon dataset is the recording acquisition frame rate, here at ~14.8 Hz, resulting in time-frame windows of ~67 ms (the Allen dataset has double this resolution, ~30 Hz). **Electron microscopy**. After functional imaging, the mouse was perfused with fixant agents, dissected, and 200 μm coronal slices of the V1 area, interested by two-photon sessions, were cut. Serial sections of 40 nm thickness were cut from the slices and prepared for transmission electron microscopy. Custom modifications to the setup and camera allowed fields-of-view as large as (13 $\mu m^2$) at 3.58 nm resolution. Data were acquired in blocks, aligned through multiple steps, and defects manually detected. Somas, synaptic cleft, and spine detection and partnering were manually performed on a (387 clefts) subset for training and testing machine learning libraries. The rest were performed by machine learning libraries. Finally, cells identified in the two-photon imaging max projection were manually co-registered with EM-identified somas.

**Allen data source**. The Allen Institute made available, through its Brain Observatory, a large dataset of neuron responses from several visual cortical areas and layers, using mouse transgenic lines expressing a Cre/Tet-dependent fluorescent calcium indicator (GCaMP6f), which allows

the recording of calcium influx associated with neural activity. The complete description of mouse transgenic lines, surgical procedures, behavior training, implants, two-photon microscope features, stimulation and recording setups, and protocols were already published (see Allen VisualCoding_Overview whitepaper in the references). Here we briefly provide the relevant information in the context of our work. **Cell type and experiment selection**. The Allen Brain Observatory contains data collected in several cell types of mouse visual cortices (see Allen VisualCoding_Genotyping whitepaper in the references). Cell-type specific expression of GCaMP6f was conferred by the Cre recombinase and tetracycline-controlled transactivator protein (tTA) under the control of the Camk2a promoter with the Ai93 and Ai94 reporters. To maximize the number of recorded neurons across layers, we selected all Cre drivers specific for pyramidal neurons and layers. Considering that each layer of mouse V1 is roughly 100um thick (Scala et al. 2019), we were able to design cell-type and layer-specific queries which resulted in the selection of the following experiment ids (as of 2019/09/10). We selected layer 2/3 planes, in order to have a dataset comparable to the one from the MICrONS project (query: http://observatory.brain-map.org/visualcoding/search/overview?area=VISp&imaging_depth=175,185,195,200,205,225,250,265,275,276,285,300&tld1_name=Slc17a7-IRES2-Cre,Cux2-CreERT2,Emx1-IRES-Cre), selected experiment ids: [502115959, 501574836, 502205092, 502608215, 510514474, 503109347, 510517131, 524691284, 645413759, 660513003, 704298735, 702934964, 712178511, 526504941, 528402271, 540684467, 545446482, 561312435, 596584192, 647155122, 652094901, 652842572, 653122667, 653125130, 657080632, 661328410, 661437140, 663485329, 679702884, 680156911, 683257169, 688678766] (with exp: 501271265 removed due to https://github.com/AllenInstitute/AllenSDK/issues/66). A total of 32 experiments were selected and downloaded as NWB files. Each experiment contained pre-processed calcium indicator fluorescence movies (512x512 pixels, i.e. 400 µm cortical field of view, sampled at 30Hz), corrected for pixel leakage during scanning, ROI filtered, and neuropil subtracted. Each resulting NWB file consisted of an experiment session (~90 min) at a given location (cortical area and depth).

**Calcium spike timing extraction**. To infer the action potential timings from the calcium indicator fluorescence of the Allen Brain data source, we used the python library OASIS (Friedrich et al. 2017). This library for spike inference, which is based on an active-set method to infer spikes, also has routines for automatic estimation of its parameters. The library is available

at https://github.com/j-friedrich/OASIS. As parameters for the deconvolve function, we used *penalty*=1, and we used the automatic estimation of fluorescence variation from the data (parameter *g*). The resulting spike timings obtained with these parameters were verified for adherence to the example deconvoluted data provided by the Allen Brain Observatory ipython notebooks.

**Dynamical analysis**. For each data source, we applied the same dynamical analysis. The analysis of synchronous irregular population events has already been developed in MATLAB™ and described in Filipchuk et al. 2022, please refer to it for an in-depth description. We reimplemented all analysis steps in Python (using the scipy and numpy libraries) and tested them against the original analysis. Briefly, after estimating spike trains with the OASIS library (see above), single cell activity was described as a cell binary vector, where the number of elements was equal to the $T$, number of time frames during the recording (frame duration was ~30ms). A value of 1 was assigned at the time frames corresponding to the onset of each spike, and the cell vector was zero otherwise. The number of cell vectors was equal to the total number of recorded neurons in the field of view, $N_e$, resulting in a $T$x$N_e$ spiketrain matrix where columns corresponded to the time frames and rows to the neurons. Each column was summed to give the number of neurons coactive at every time frame from which the instantaneous population firing rate could be deduced. As is visible from sample raster plots (Fig. 1A), there were periods of time where spikes were much more synchronized across the population, which could be interpreted as population events, departing from the fluctuations of an asynchronous population spiking process. To identify whether the population events were above chance coincidence, and determine their exact start and end, we applied the following algorithm. (**1**) We created 100 surrogate $T$x$N_e$ spiketrain matrices by reshuffling each neuron's inter-spike interval. The average 99 percentile across time frames was then calculated and a firing rate threshold for event significance was obtained by adding this average value to a local baseline estimate that aimed at correcting slow fluctuations of background firing rate. The baseline estimate was generated using an asymmetric least squares smoothing algorithm from Eilers and Boelens (2005), with parameters $p=0.01$ for asymmetry and $\lambda=10^8$ for smoothness. (**2**) Experimental population firing rate trace was smoothed using Savitzky-Golay filtering, with order=3 and frame window=7, to get rid of non-essential peaks. Local maxima for the smoothed curve that were above the previously defined threshold were retained (Fig. 1B, inset, red square). The adjacent local

minima around each of the local maxima were identified (Fig. 1B, inset, green circles). Their time frames were taken as the beginnings and ends of population events (Fig. 1A, limits of the green vertical band). (**3**) The time interval between the beginning and end of each population event defined its duration. We described each population event as a binary vector of length equal to the total number of neurons in the recorded field of view ($N_e$). We initialized all vector's elements to *0*, and then we indicated the participation of a cell to the event, spiking at least once over its duration, with a coordinated *1* (Fig. 1A, left). (**4**) Pearson's correlation matrix for ongoing and evoked events was constructed by computing the Pearson correlation coefficient between all binary vectors. In plotting the matrix, the color reflected the degree of correlation with a colormap ranging from 0 to 1. (**5**) Population events sharing a substantial number of neurons, i.e. having a significant degree of correlation, were clustered together (using agglomerative linkage clustering with the farthest distance based on correlation metric, from the python *scipy.clustering* package), and the correlation matrix could be permuted according to the clustering order (Fig. 1C). (**6**) The correlation between population events might be simply due to the finite number of recorded cells. We, therefore, defined a significance threshold for intra-cluster correlation, established using surrogate events. We generated $100 \times N_e$ surrogate event vectors (with the same number of cells per event of the originals, but randomly chosen cells, without replacement). We then performed correlation-based clustering (as in point 5) of the resulting surrogate clusters, and we used the 95 percentile of correlation coefficient of these clusters as a correlation threshold. (**7**) To quantify the pattern reproducibility of events within a cluster, i.e. the number of cells shared across events in a cluster, the correlation was calculated across all events of each cluster. (**8**) Core cells were identified as those participating in >95% of the events within each cluster (relaxing this requirement even to 75%, to allow for a more participative definition of cores, did not change the statistics presented in Fig. 2, see Fig. S6). Once identified, we discarded cores that had a high unspecific firing, by verifying that the average firing rate within events was higher than that outside events.

The whole analysis workflow code, including the calls to download the data through the AllenSDK, is available on GitHub (https://github.com/dguarino/GuarinoFilipchukDestexhe), including also a Docker container for faster reproducibility (https://hub.docker.com/repository/docker/dguarino/GuarinoFilipchukDestexhe).

**Structural analysis**. We used the data tables published by the MICrONS project on their website and the referenced publications (see above). **Postsynaptic spine number and volume analysis**. We selected the subset of proofread synapses having as soma root id those identified and co-registered in the two-photon dataset. After the dynamical analysis was performed (see above), core neuron ids for each event were available and used to query the synapse table, and postsynaptic spine volumes were collected by identified type (core or non-core). The four possible combinations (core-core, core-other, other-core, other-other) were plotted in Fig. 2. Differences in significance and effect size were established using Kruskal-Wallis and Kolmogorov-Smirnov distance, since the distributions were non-normal, as reported below in the statistical methods. **Synaptic functional efficacy analysis**. To estimate functional connectivity, we adopted the same method described in Sadovsky and MacLean (2013). Briefly, an adjacency matrix representing a graph for each experiment was created with nodes being all recorded cells, and directed edges formed according to a single frame lagged correlation (frame duration: 67.4ms) and weighted according to the number of spikes (see supplementary figure 1). **Graph theory analyses**. An adjacency matrix was built by coordinating pre- and post- soma root ids. All graph analyses reported in Fig. 2 were performed using the python version of the library iGraph (Csárdi and Nepusz 2006). The iGraph library allows motif identification with either 3 or 4 nodes. We used 3-motifs to be able to compare our results with other publications and with the online MICrONS ipython notebooks, and also to make computations of the 100 surrogate graphs run in a reasonable time. The comparison of core-based cycles and other-based cycles was performed over an adjacency list and using a function that recursively checked over the list of neighbors starting with each core (or non-core) cell id.

**Statistical methods**. We used the D'Agostino and Pearson's test for normality (of the *scipy* library) to evaluate the distributions resulting from our measurements of the nominal variables (spine volumes, 1-lag correlations, degrees, betweenness, …). For normally distributed variables, we used the One-way ANOVA test. For non-normally distributed variables, we adopted the Kruskal-Wallis test. For some of the variables, the sample size was large (beyond 100 samples), therefore even small variations could be labeled as significant. In these cases, a quantitative measure of the effect size was required. We adopted, as a measure of effect size, the Kolmogorov-Smirnov test difference, which is more robust than Cohen's delta for non-normal distributions (Wilcox and Keselman 2003).

**Neuron model**. All simulated networks were composed of n=12500 (10000 excitatory and 2500 inhibitory) conductance-based adaptive exponential integrate-and-fire (AdExIF) point neurons. The set of equations describing the membrane potential (1) and spike adaptation current (2) of a neuron are

$$C_m \frac{dV}{dt} = -g_L(V - E_L) + g_L \Delta \, exp[(V - V_T)/\Delta] - w/S \quad (1)$$

$$\frac{dw}{dt} = \frac{1}{\tau_w}[a(V - E_L) - w] \quad (2)$$

with $C_m$ being the membrane capacitance (nF), $g_L$ the resting (leak) conductance (μS), $E_L$ the resting (leak) potential (mV, which is also equal to the reset value after spike), Δ the steepness of the exponential approach to the threshold (mV), $V_T$ the spike threshold, and $S$ membrane area (μm$^2$). When $V$ reaches the threshold, a spike is emitted and $V$ is instantaneously reset and clamped to the reset value during a refractory period (ms). $w$ is the adaptation variable, with time constant $\tau_w$ (ms), and the dynamics of adaptation is given by parameter $a$ (in μS). At each spike, $w$ is incremented by a value $b$ (in nA), which regulates the strength of adaptation. An experimentally informed parameter set was chosen (from Zerlaut et al. 2011) and kept fixed, see Table 1.

| Parameter | Value | |
|---|---|---|
| **Regular Spiking (excitatory)** | | |
| Threshold ($V_T$) | -50.0 | mV |
| Resting potential ($E_L$) | -65.0 | mV |
| Afterpotential reset | -65.0 | mV |
| Refractory time constant | 5 | ms |
| Membrane time constant ($\tau_m$) | 15.0 | ms |
| Membrane capacitance ($C_m$) | 0.15 | nF |
| Subthreshold adaptation ($a$) | 4.0 | nS |
| Spike-triggered adaptation ($b$) | 0.02 | nA |
| Slope factor ($\Delta_T$) | 2.0 | mV |
| Adaptation time constant ($\tau_w$) | 500 | ms |
| **Fast Spiking (inhibitory)** | | |
| Threshold ($V_T$) | -50.0 | mV |
| Resting potential ($E_L$) | -65.0 | mV |
| Afterpotential reset | -65.0 | mV |
| Refractory time constant | 5 | ms |

| | | |
|---|---|---|
| Membrane time constant ($\tau_m$) | 15.0 | ms |
| Membrane capacitance ($C_m$) | 0.15 | nF |
| Subthreshold adaptation ($a$) | 0.0 | nS |
| Spike-triggered adaptation ($b$) | 0.0 | nA |
| Slope factor ($\Delta_T$) | 0.5 | mV |
| Adaptation time constant ($\tau_w$) | 500 | ms |

**Table 1. Parameters of the AdEx Integrate-and-Fire model**.

**Synapse model**. The synaptic connections between neurons were modeled as transient conductance changes. The synaptic time course was modeled as an alpha function with a fast rise followed by an exponential decay:

$$\tau_{syn} \frac{dg_{syn}(t)}{dt} = -g_{max}(t - S_{syn}(t))\, exp[-(t - S_{syn}(t)) - \tau_{syn}] \quad (3)$$

where $syn \in \{exc, inh\}$, $S_{syn}(t)=\delta(t - t_k)$ are the $k$ incoming synaptic spike trains where $i \in \{1, .., N\}$ refers to presynaptic neurons and k to the different spike times of these neurons. The synaptic time constants were chosen to be $\tau_{exc}$=3 ms and $\tau_{inh}$=7 ms for excitation and inhibition respectively. The reversal potentials were $E_{exc}$=0 mV and $E_{inh}$=−80 mV. The synaptic weights $g_{syn}(t)$ were set to $g_{exc}$=1 nS for the excitatory conductance, and a balance of $g_{inh}$=5 nS unless stated otherwise. We used a constant delay of 0.5 ms, equal for all connections.

**Network architecture**. We simulated a microscope focal plane area of $L$=500 μm$^2$ as a 2D-layer-like network with periodic boundary conditions and an excitatory/inhibitory neuron ratio of 4:1. Neurons were arranged on a grid of 5 μm steps. Every neuron was sparsely connected with the rest of the network with a connection probability drawn from distance-dependent probability distribution. Each neuron was connected with other network neurons depending on their distance $r_{ij}$, according to an exponential profile:

$$p_{ij} = A_{syn} * exp^{-(\lambda_{syn} r_{ij})} \quad (4)$$

where $A_{syn}$ is the amplitude of the exponential, varying the number of neurons sampled in the chosen radius $r_{ij}$. The amplitudes $A_{syn}$ were set to have the number of connected neurons roughly match the distributions described by Katzel et al. 2011, Markram et al. 2015, and Seeman et al. 2018, considering the topological distribution and the excitatory/inhibitory neuron ratio

($A_{exc\text{-}exc}$=14, $A_{exc\text{-}inh}$=24, $A_{inh\text{-}exc}$=14, $A_{inh\text{-}inh}$=24), resulting in a degree of ~75 connections per neuron. The decay controller $\boldsymbol{\lambda}_{syn}$ was set to $\boldsymbol{\lambda}_{exc}$=1.2 and $\boldsymbol{\lambda}_{inh}$=1.5. The seed to the random number generator responsible for the sampling of the connections was systematically varied, producing N=20 different networks, but following the same type of exponentially decaying distributions.

**Drive**. An external population of Poisson drivers was connected to both the RS and FS populations, with uniform random probability drawn from the half-open interval [0,0.01), with a fixed synaptic weight of 0.5 nS.

**Simulator**. All simulations were performed using the NEST simulator (Diesmann and Gewaltig 2001) controlled through the PyNN interface (Davison et al. 2009).

## Supplementary Figures

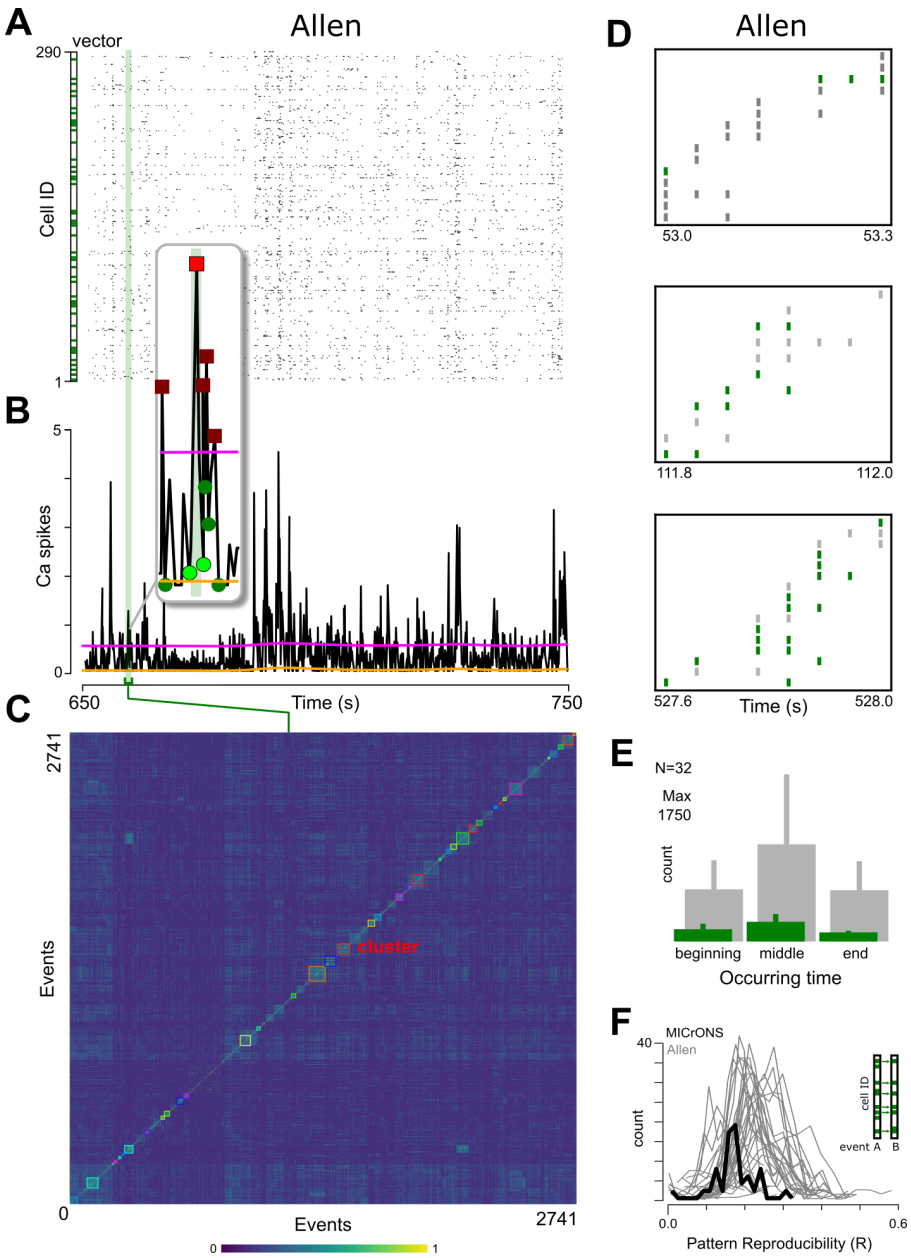


**Fig. S1. Comparison of MICrONS and Allen Brain Observatory events**. (**A-E**) As for Fig. 1, Fig. 1. (**A**) Calcium spikes raster plot from an example experiment (ID: 540684467). (**B**) Population events. (**C**) Clustered matrix of correlations between population vectors. More events and structure is present in the Allen dataset. However, the stimuli were different (see Allen whitepapers). (**D**) Example events from Allen dataset. (**E**) Core neurons (green) were evenly distributed along events. (**F**) Distributions of pattern reproducibility for the MICrONS phase 1 dataset (black) and each (*N*=32) Allen Brain Observatory (gray). The MICrONS distribution does not qualitatively differ from those from the Allen Brain Observatory. Note that Allen

recordings are on average three times longer than the MICrONS, resulting in a reduced count for the latter.

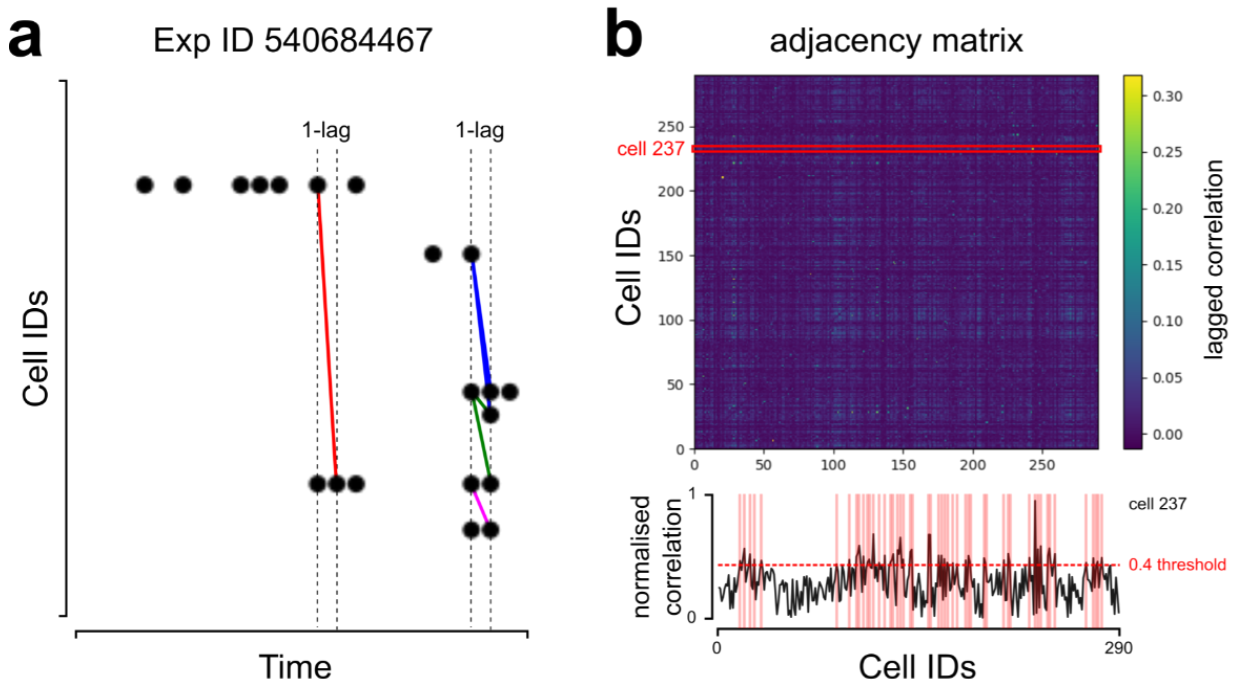


**Fig. S2. Structural quantitative characterization from in-vivo awake cortex**. (**A**) Detail from experiment id 540684467 raster plot showing calcium spikes (black circles). Each row contains the calcium spikes for a cell. The minimal interval between two spikes is the two-photon imaging time resolution (30 Hz for the Allen Brain dataset). This interval represents the 1-lag correlation interval to identify cells potentially connected. In the figure, only some cells with 1-lag correlated firing were joined by colored segments to improve legibility. (**B**) The vector of 1-lag correlations for each cell is collected into a matrix (top). Weak correlations (threshold=0.4) were not considered for further analysis (bottom, correlations for cell id 237).

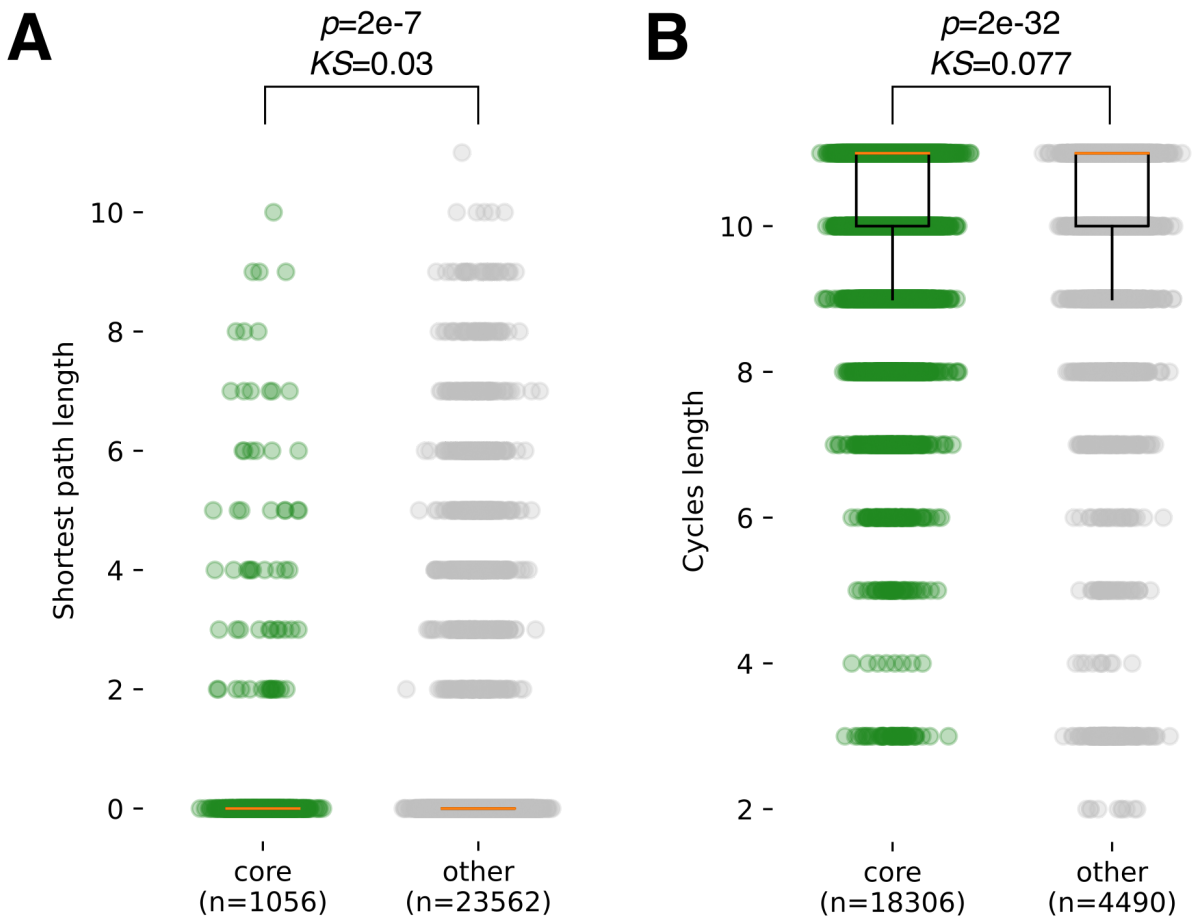


**Fig. S3. Cores are not recursively connected via multi-synaptic feedback**. Even if cores were not directly connected, they could be highly connected via secondary paths, abundant enough to ensure that they are pattern completion units in traditional attractor network terms. (**A**) Core-to-core shortest paths were neither more nor shorter than other-to-other paths (0.27±1.19 vs 0.16±0.92 length, Kruskal-Wallis t=26.4 p=2.7e-07, *KS*=0.030.) (**B**) Core neurons could be part of looped paths, circling back to them, and providing a weak form of recursion. Core-based cycles were more (green, 18306) compared to other-based cycles (gray, 4490). But core and non-core cycles had on average the same length (10.34±1.07 and 9.93±1.76 connections, with minimal effect size KS=0.077), same as the network diameter (*d*=10).

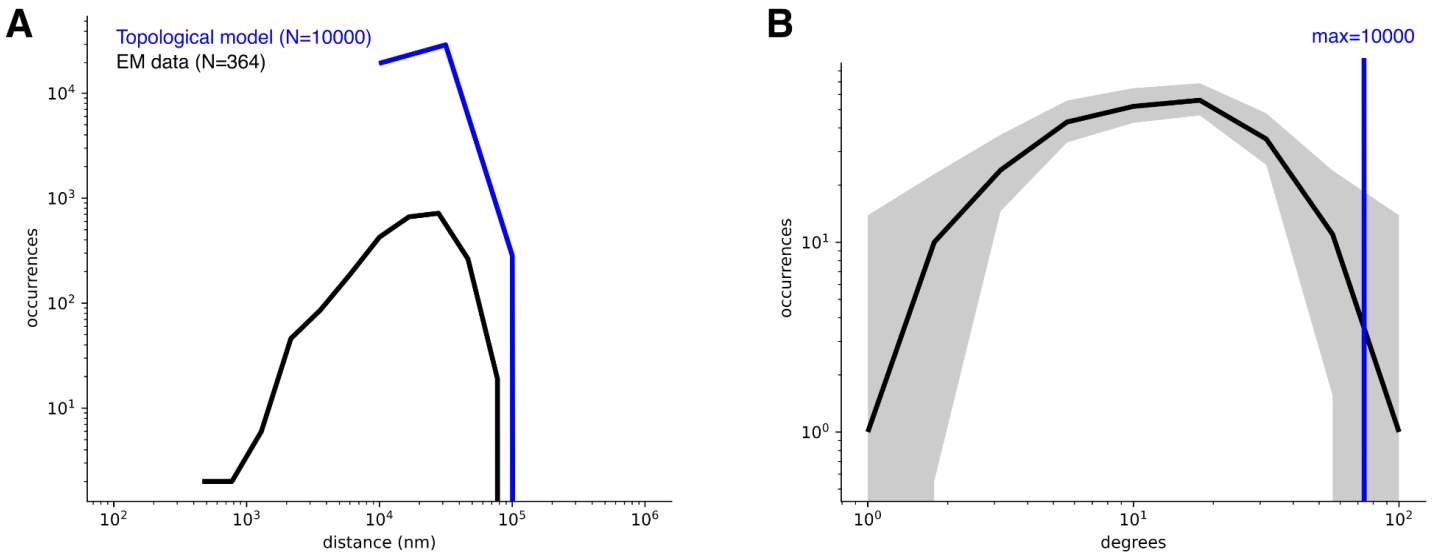


**Fig. S4. Model units distances and degrees were loosely based on the EM data**. (**A**) We took the full list of EM-identified cells (black) to have the largest number of inter-somatic distances. Given the structure of our topological model (500 $\mu m^2$ with 5 µm grid step) the minimal distance between model neurons is 5000 nm (blue). (**B**) The number of connections per neuron in the EM data followed a heavy-tailed distribution peaking at 20 connections per neuron (black, with grayed bootstrapped confidence interval). Our topological model had a fixed 75 connections per neuron (blue), towards the upper end of the EM distribution.

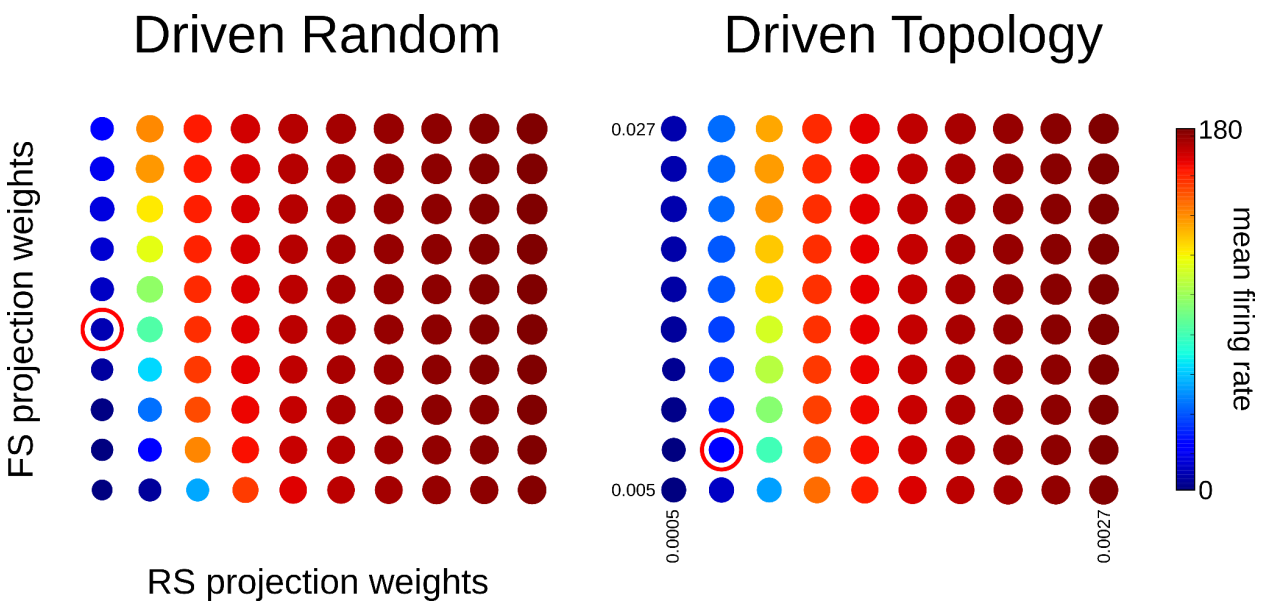


**Fig. S5. The model is stable with respect to changes in synaptic parameter space**. We explored the parameter space made by the relationship between regular spiking (RS) and fast spiking (FS) synaptic conductance change triggered by incoming spikes, for both the randomly connected (*left*) and topologically connected (*right*), for what concerns the stability of firing regime. Many couples of synaptic parameters produced stable firing rates too high to be comaprable with the 2-photon activities (from 80 spikes/s on, from cyan to red, see colorbar on the right). We therefore further tested several couples below 80 spikes/s and settled on 5-10 spikes/s (marked by the red circle).

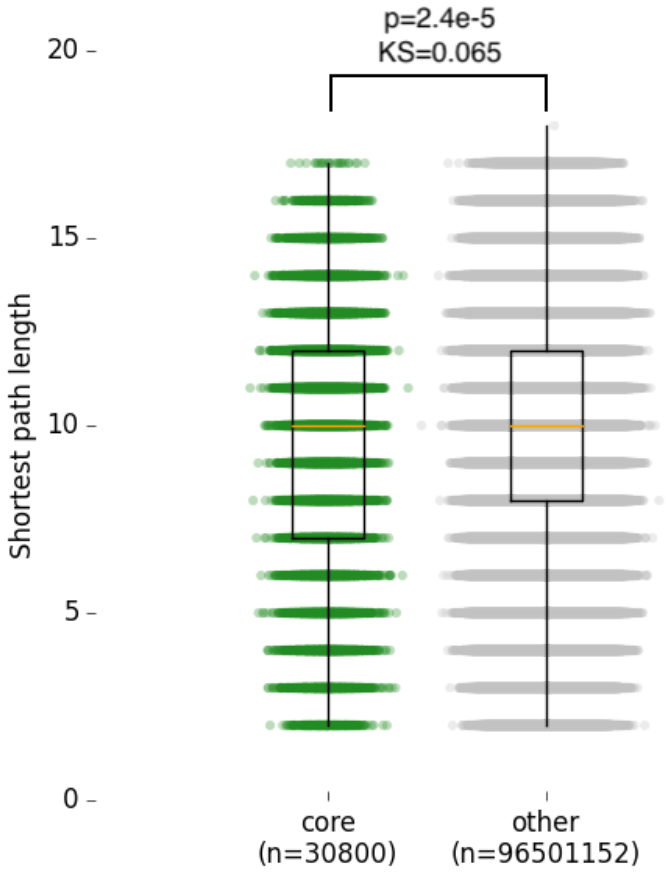


**Fig. S6. The shortest paths between model cores and others were not different.** Even if cores were not directly connected, they could be highly connected via secondary paths, abundant enough to ensure that they are pattern completion units in traditional attractor network terms (see the works of Amit). To evaluate this aspect also in the model as in the data (see Fig. S2), we measured the number and length of shortest paths between cores and compared them with those made by others. We found that the shortest paths between cores were significantly shorter compared to those between others (cores: 9.75±3.36 vs others: 10.04±2.98 length), overall with negligible effect size (*KS*=0.065). A direct comparison of cycles in the model is computationally unfeasible.

.

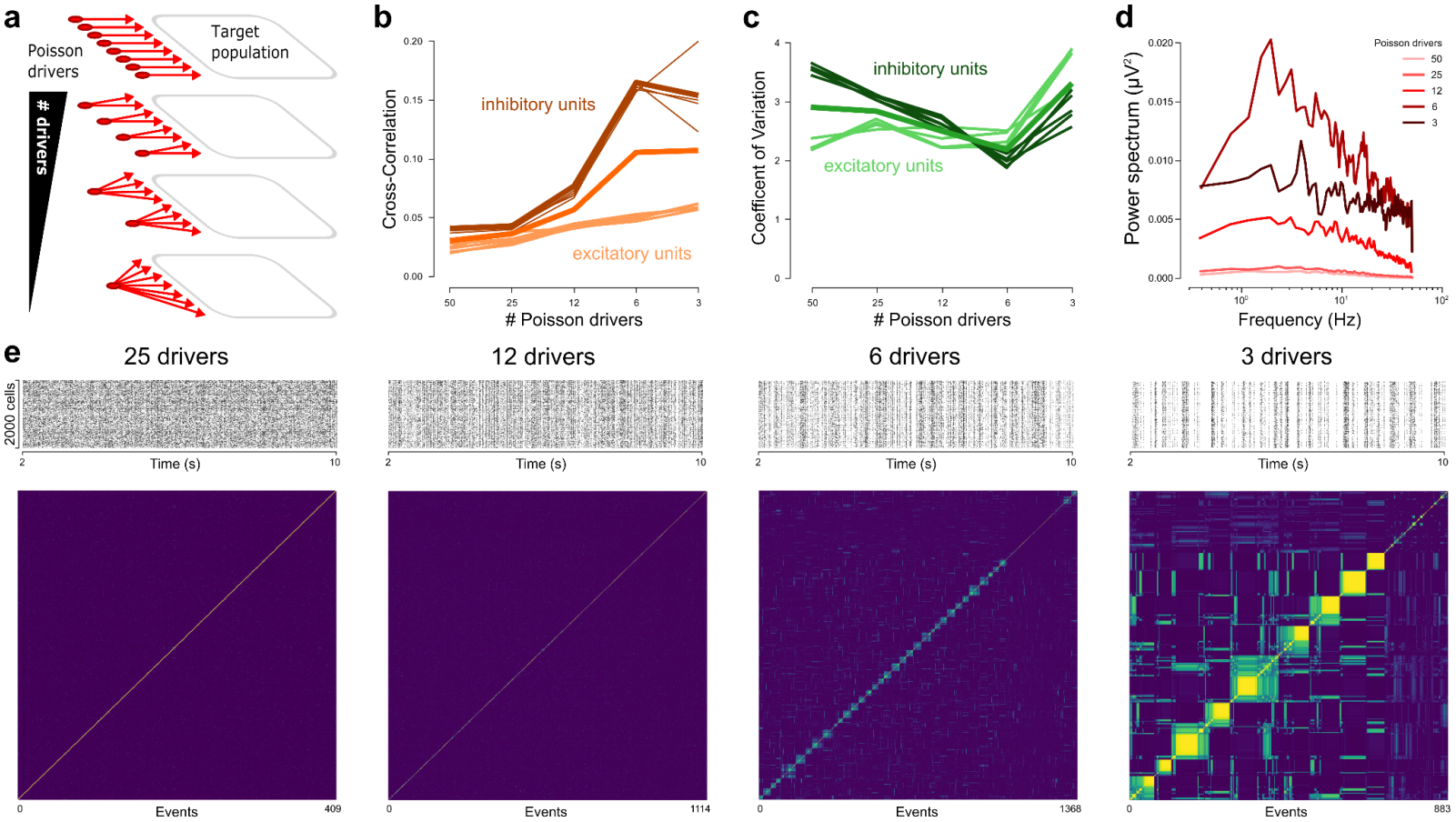


**Fig. S7. Increasing input correlations brings the model towards oscillatory regimes**. (**a**) For the same target population (right), we systematically reduced the number of Poisson input drivers (red disks and arrows), to explore how the increase in input correlations affected the correlations between population events. (**b**) Reducing the number of Poisson input drivers (n=[50, 25, 12, 6, 3]) increased the population cross-correlation of spikes towards values characteristic of oscillating regimes (from CC=0.035 at n=50, to CC=0.11 at n=3). (**c**) Reducing the number of Poisson input drivers did not significantly affect the population coefficient of variation (Kruskal-Wallis test, p=0.21). (**d**) Reducing the number of Poisson input drivers increased the power for slow oscillations in the Fourier spectrums of the firing rates. (**e**) Four example 10 sec spike rasters for 2000 example cells, with their correlation matrices, showing the changes in firing regimes responsible for the increase in population events correlation.